Magnetic phase diagrams of $L_{1-x}A_xMnO_3$ manganites (L=Pr,Sm; A=Ca,Sr)

C. Martin, A. Maignan, M. Hervieu, and B. Raveau
Laboratoire CRISMAT, UMR 6508 associée au CNRS, ISMRA et Université de Caen 6, Boulevard du Maréchal Juin, 14050 Caen Cédex, France

(Received 4 June 1999)

The magnetic phase diagrams of four $L_{1-x}A_xMnO_3$ series (L=Pr,Sm; A=Ca,Sr) have been established combining neutron diffraction, electron microscopy, and magnetotransport measurements in order to understand and optimize the colossal magnetoresistance (CMR) properties of these compounds. A complementary study of the $La_{1-x}Ca_xMnO_3$ phase diagram ($x \geq 0.8$) is also performed. The comparison of these diagrams demonstrates that low $\langle r_A \rangle$ values are required to obtain CMR properties on the Mn^{4+} rich side, i.e., when a competition between charge order and cluster glass phases occurs ($L_{1-x}Ca_xMnO_3$; L=Pr,Sm). As a consequence of the low $\langle r_A \rangle$ values on the rich Mn^{3+} side ($x<0.5$ in $L_{1-x}Ca_xMnO_3$), the ferromagnetic metallic (FMM) state is never reached, whereas for the same x values, systems with larger $\langle r_A \rangle$ ($L_{1-x}Sr_xMnO_3$; L=Pr,Sm) exhibit CMR properties related to the FMM state. A particular attention is paid to the $x \sim 0.5$ compositions of these $L_{1-x}Sr_xMnO_3$ series for which the Curie and Néel temperatures are $T_N < T_C$ and $T_C < T_N$ for Pr and Sm, respectively. The importance of the chemical factors on the charge ordering (studied vs temperature by electron diffraction) and on the magnetic structures (from neutron diffraction) is also emphasized. [S0163-1829(99)11241-4]

I. INTRODUCTION

The recent studies of the perovskite manganites $L_{1-x}A_xMnO_3$ (L=lanthanide; A=alkaline earth) have shown that their colossal magnetoresistance (CMR) properties are greatly governed by the sign and concentration of the charge carriers. In the hole doped compositions, i.e., for Mn^{3+} rich manganites ($x<0.50$), the double exchange (DE) Mn^{3+}-O-Mn^{4+} ferromagnetic (FM) interactions predominate.[1–3] Consequently, for these hole doped manganites, the CMR effect results from a magnetic field induced transition, from a paramagnetic insulator (PMI) to a ferromagnetic metal (FMM).[4–5] Polarons formation, linked to the presence of the Mn^{3+} Jahn-Teller species, is responsible for the activated regime in the paramagnetic state. In contrast to the hole doped manganites, the electron doped ones $L_{1-x}Ca_xMnO_3$, i.e., the Mn^{4+} rich compounds ($x>0.50$), exhibit only a narrow range of compositions, around the critical value $x_{cr} \cong 0.80-0.90$, where the CMR effect is observed.[6–9] In fact, for $x<x_{cr}$ there exist charge ordering (CO) phenomena of the Mn^{3+} and Mn^{4+} species together with antiferromagnetic insulating (AFMI) state, whereas for $x>x_{cr}$ ferromagnetism (FM) or cluster glass (CG) appears concomitantly with charge delocalization (metallicity). Thus, for x_{cr}, a competition between CO-AFMI and FM phenomena is observed, and the AFM state can be collapsed into the FM metallic state by applying a magnetic field, so that an insulator to metal (IM) transition is induced, leading to the CMR effect.

Although this description is oversimplified, it emphasizes the great differences which exist between the Mn^{3+} and the Mn^{4+} rich sides of the solid solution, so that the properties of the hole doped side cannot be simply transposed to its electron doped counterpart. This can be easily seen on the phase diagram of $La_{1-x}Ca_xMnO_3$ that has been previously published.[10,11]

Moreover, the properties of the manganites are not only sensitive to the manganese valency but are also strongly affected by chemical factors such as average A-site cationic radius $\langle r_A \rangle$ (Refs. 12–14) and A-site cationic size mismatch[15,16] which is quantified by the variance σ^2 of the ionic radii.[15] For instance, keeping the hole concentration constant in the Mn^{3+} rich FM compositions, it has been shown that a decrease of $\langle r_A \rangle$ tends to diminish the Mn-O-Mn angle, reducing the bandwidth (W), and consequently T_C.[13] In contrast, a small $\langle r_A \rangle$ value is required for the appearance of CMR in Mn^{4+} rich manganites.[9] Finally, whatever $\langle r_A \rangle$ and manganese valency are, the increase of σ^2 tends to depress the magnetic interactions, FM or AFM, and to destabilize CO.[15–17] These few examples show the great complexity of the relationships between the chemical factors ($\langle r_A \rangle$, σ^2, carrier nature, and concentration) and the magnetotransport properties of the manganites. Thus, the understanding of the CMR properties in these oxides, and especially their optimization, requires the knowledge of the magnetic phase diagrams of several series of $L_{1-x}A_xMnO_3$ perovskites.

In this paper, we present the magnetic phase diagrams of four different series of manganites $L_{1-x}A_xMnO_3$. The first series $Sm_{1-x}Ca_xMnO_3$ (labeled SmCa), which corresponds to low $\langle r_A \rangle$ (1.132–1.18 Å) and small σ^2 ($<5.8 \times 10^{-4}$ Å^2), exhibits CMR only on the electron doped side. The second series $Pr_{1-x}Ca_xMnO_3$ (PrCa), characterized by the absence of size mismatch, i.e., a constant $\langle r_A \rangle$ value (1.18 Å), shows CMR on both sides, hole doped and electron doped regions. The third series, $Sm_{1-x}Sr_xMnO_3$ (SmSr), which corresponds to large $\langle r_A \rangle$ values (1.132–1.310 Å) and the highest σ^2_{max} value (7.9×10^{-3} Å^2), exhibits CMR mainly on the hole doped side, i.e., for x ranging from 0.20 to 0.52. The fourth series, $Pr_{1-x}Sr_xMnO_3$ (PrSr), characterized by larger $\langle r_A \rangle$ values (1.18–1.310 Å) and smaller size

mismatch ($\sigma^2_{max}=4.2\times10^{-3}$ Å^2) than the SmSr line, also shows CMR, mainly on the hole doped side, i.e., for x ranging from 0.25 to 0.55. Based on magnetic and transport measurements, we discuss herein the evolution of the ferromagnetic and antiferromagnetic regions versus chemical parameters (σ^2,$\langle r_A\rangle$) and manganese valency (carrier concentration and nature). In order to allow a comparison, the series $La_{1-x}Ca_xMnO_3$ (LaCa) first studied by Schiffer *et al.*[10] has been completed on the Mn^{4+} rich side, showing the existence of CMR in both the hole and electron doped sides.

II. EXPERIMENT

The preparation of these polycrystalline samples, in air at 1500 °C, has been reported elsewhere.[8,9,14,16] For both calcium series, $Sm_{1-x}Ca_xMnO_3$ and $Pr_{1-x}Ca_xMnO_3$, it was possible to study the $0.1\leqslant x\leqslant 1$ lines, whereas for the $L_{1-x}Sr_xMnO_3$ series the solubility line is limited to $0.1\leqslant x<0.9$. In fact, it is necessary to modify the synthesis procedure for $L_{1-x}Sr_xMnO_3$ with $x\geqslant 0.9$ (by using Ar flow at high temperature) to obtain a perovskite exhibiting only a cubic mode of the layer stacking along $[111]_p$, without any hexagonal defective layers or complex polytypes as usually observed in the $SrMnO_{3-\delta}$ phases. To avoid to change the synthesis conditions, the studies of the $L_{1-x}Sr_xMnO_3$ series are limited to $x=0.9$. On the opposite side, the $x=0$ compositions, i.e., $SmMnO_3$ and $PrMnO_3$, are difficult to prepare as stoichiometric phases following our experimental conditions, so that these compositions have also been excluded. The purity of the samples has been checked by x-ray powder diffraction with a Philips diffractometer and by electron diffraction (ED) carried out with Jeol 200CX and 2010 microscopes. EDS (energy dispersive spectroscopy) analyses confirm that the cationic compositions are homogeneous and close to the nominal ones; iodometric titrations show an oxygen content of O_3.

The T dependence of the magnetization (M) is registered with a vibrating sample magnetometer [zero field cooled (ZFC) 1.45 T, from 4 to 300 K] or with a SQUID magnetometer with the same field up to 400 K and the resistivity data are collected on bars by a four-probe method upon cooling the samples from 400 K down to 5 K in 0 and 7 T. All the transition temperatures given in the following phase diagrams have been extracted from the $M(T)$ curves. In some cases, their values are confirmed by electron and/or neutron diffraction versus T studies.

III. RESULTS

A. $Sm_{1-x}Ca_xMnO_3$: A series with CMR properties only on the electron doped side

This series is characterized by low $\langle r_A\rangle$ values, ranging from 1.132 to 1.180 Å, i.e., from $x=0$ to $x=1$. The tolerance factor of these perovskites is always lower than 1 and increases with x (calcium content). These samples exhibit thus highly distorted $GdFeO_3$-type structures, that are favorable for the charge localization and detrimental for the DE interactions. Consequently, no ferromagnetic metallic state can be detected in all the hole doped region, as shown from the magnetic phase diagram of this system (Fig. 1). Nevertheless, a ferromagnetic insulating (FMI) domain is observed for $x<0.35$. The magnetization at 4 K increases with x, reaching a maximum value of $2.5\mu_B$ at $x=0.20$, and decreasing abruptly again (see dashed line Fig. 1). This ferromagnetism, deduced from the $M(T)$ curves (inset of Fig. 2), is not sufficient to allow a delocalization of the carriers, so that even under 7 T, the resistivity behavior cannot be forced to metallicity and no CMR properties are obtained in this region.

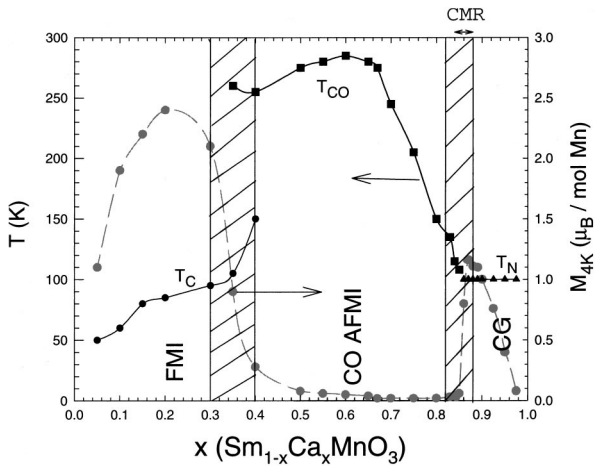

FIG. 1. Magnetic phase diagram for the $Sm_{1-x}Ca_xMnO_3$ series. ●, ■, and ▲ are for T_C, T_{CO}, and T_N, respectively. The gray symbols and dashed line are the magnetization values registered at 4.2 K in 1.45 T. The two hatched zones represent the intermediate regions, and the CMR domain is noted by arrows in the upper part.

For $0.35\leqslant x\leqslant 0.80$, the electron diffraction (ED) study vs temperature shows that different charge ordered structures are stabilized at low temperatures ($T<T_{CO}$).[18] The as obtained T_{CO} temperatures are in good agreement with the values deduced from the $M(T)$ [Fig. 2(a)] and $\rho(T)$ curves [Fig. 2(b)], which evidence AFM states and activated as resistivities. Thus, this charge ordered domain coincides with a large AFMI region, but unfortunately T_N values could not be systematically determined from neutron diffraction due to the neutrophagic character of samarium. Note that T_{CO} is not maximum for the half-doped composition $x=0.50$, but for $x=0.60$.

For $0.86\leqslant x\leqslant 0.92$, corresponding to the electron doped side (Mn^{4+} rich region) magnetization values of about $1\mu_B$ at 4 K are shown [Figs. 2(a) and 1]. The magnetic state, as revealed by ac-χ measurements, is characteristic of a cluster glass (labeled CG on Fig. 1) in this composition domain and the $\rho(T)$ curves show semimetallic behavior ($\rho_{5K}<10^{-3}\,\Omega$ cm for $x=0.90$, for instance, inset of Fig. 2(b).[19] At the frontier between the CG and CO-AFMI domains, there exists a narrow range of composition ($x\sim0.85$) where CMR properties can be observed.[8,9] Consequently, two compositions [$x=0.90$ (CG) and $x=0.85$ (CMR)] have been selected for a neutron diffraction (ND) study by using Sm^{152}. Both compounds exhibit a Pnma structure in the paramagnetic state at room temperature but the low temperature phases are quite different. At 10 K, $Sm_{0.15}Ca_{0.85}MnO_3$ exhibits a $P2_1/m$ space group associated with a C-type AFM structure and $Sm_{0.10}Ca_{0.90}MnO_3$ is characterized by a Pnma space group with a G-type AFM structure with a FM

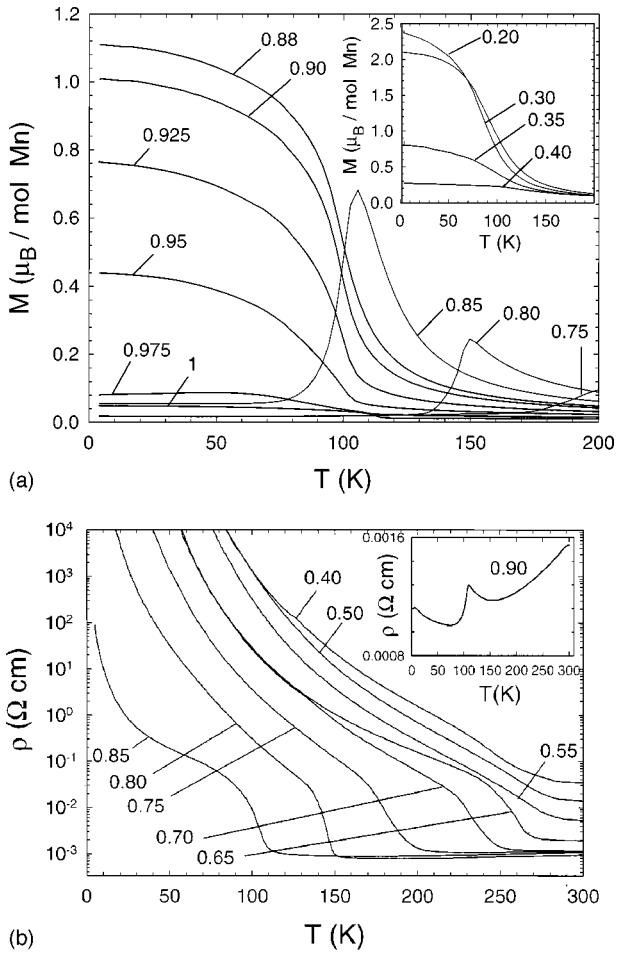

FIG. 2. (a) T dependent magnetization (M) curves registered upon heating in 1.45 T after a zero field cooling process for the $Sm_{1-x}Ca_xMnO_3$ samples, x values ($x>0.7$) are labeled on the graph. Inset: $M(T)$ curves for FM compounds of this series (with smaller x values). (b) T dependent resistivities (ρ) for the corresponding series. Inset: $\rho(T)$ curve for $Sm_{0.1}Ca_{0.9}MnO_3$.

component.[20,21] In both cases, the PM-AFM temperature transitions determined by the ND study are in good agreement with those determined on the $M(T)$ or $\rho(T)$ curves. For instance, for $Sm_{0.15}Ca_{0.85}MnO_3$, the MI transition observed around 115 K corresponds to the coupled structural (monoclinic distortion) and magnetic (C-type) transitions.[20] These observations, in the SmCa system, are close to those reported previously by Jirak for $Pr_{1-x}Ca_xMnO_3$.[22]

B. $Pr_{1-x}Ca_xMnO_3$: A series with fixed $\langle r_A \rangle$

The identical size of Ca^{2+} and Pr^{3+} cations makes that $\langle r_A \rangle$ is nearly constant (1.18 Å) and there is a very low mismatch whatever x. Thus, this diagram gives a good idea about the role of the charge carriers for a small A-site cation. Note, however, that, due to the Mn^{3+}/Mn^{4+} variation with x, the cell volume decreases as x increases. The phase diagram of this series (Fig. 3) can be compared with that of the $Sm_{1-x}Ca_xMnO_3$ series (Fig. 1), which exhibits a smaller $\langle r_A \rangle$ value, i.e., a smaller tolerance factor, for a same x value.

It can be seen that the FMI domain of this system is close to that observed for SmCa, x ranging from 0.10 to 0.30. Nevertheless the T_C values are slightly higher than those

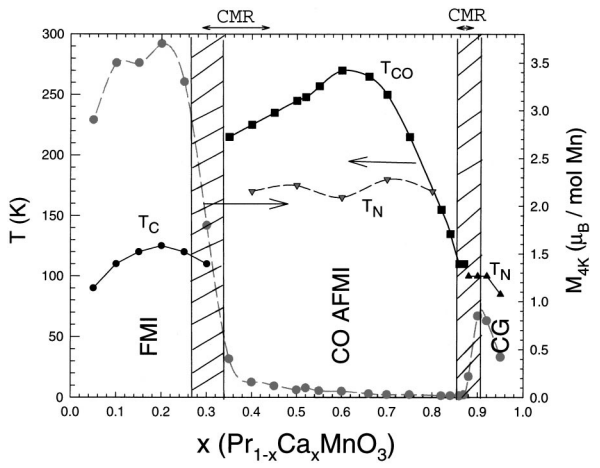

FIG. 3. Magnetic phase diagram of the $Pr_{1-x}Ca_xMnO_3$ line. ▽: the T_N values determined from ND (Ref. 22).

obtained for the first system, in agreement with the larger $\langle r_A \rangle$ values and the absence of mismatch. Correlatively, the magnetic moment at 4 K is significantly higher for $Pr_{1-x}Ca_xMnO_3$ than for $Sm_{1-x}Ca_xMnO_3$, reaching a maximum value of $3.7\mu_B$ at $x=0.20$ (see dashed gray line Fig. 3).

As for SmCa, the combined ED and magnetic study shows that the PrCa system exhibits a large charge ordered region, x extending from 0.30 to 0.80. Note that for this system, as in the SmCa series, the higher T_{CO} value is obtained for $x=0.60$ and not for $x=0.50$. The previous neutron diffraction investigations[22] show that the AFMI state coincides with the CO domain, i.e., $0.30<x\leqslant 0.8$, but $T_N \leqslant T_{CO}$ (see dashed black line with triangles on Fig. 3, from NPD of Ref. 22) and various magnetic structures are observed (CE in the middle part and C towards high x values).

The magnetic and transport measurements of the Mn^{4+} rich side[19] finally show the existence of a metallic cluster glass domain (CG), for $0.89\leqslant x\leqslant 0.92$, characterized by a magnetization maximum around $x=0.90$. This sample, studied by ND, exhibits, similarly to $Sm_{0.10}Ca_{0.90}MnO_3$, a G-type AFM structure with a FM component.[21]

Though the $\langle r_A \rangle$ value is not sufficient to obtain a FMM behavior in the hole doped region, CMR effects in 6 T magnetic fields are observed in the $0.3\leqslant x\leqslant 0.45$ range.[23] It must be pointed out that the largest effect is not obtained for the most FM sample ($x\sim 0.2$ from the $M_{4\,K}$ values on Fig. 3) but rather close to $x=0.30$, composition that lies on the borderline between AFM-CO and FMI regions. This outlines the role of remaining insulating CO regions, that can be easily magnetically collapsed leading to an increase of the CMR effect. Lattice images obtained by electron microscopy on $Pr_{0.7}Ca_{0.3}MnO_3$ at 92 K clearly show the coexistence of small ordered (CO) and not ordered regions. It is observed that the transition between CO and not ordered regions can be induced not only as a function of T but also by electron irradiation, according to a mechanism proposed in Ref. 24. On the opposite side of this line, CMR properties are also observed for Mn^{4+} rich compositions, $x\approx 0.87$,[9] for a narrow region of compositions, as in $Sm_{1-x}Ca_xMnO_3$, between CO-AFMI and CG samples.

The great similarity of both $L_{1-x}Ca_xMnO_3$ diagrams (Figs. 1 and 3) is related to their close $\langle r_A \rangle$ and A-site cat-

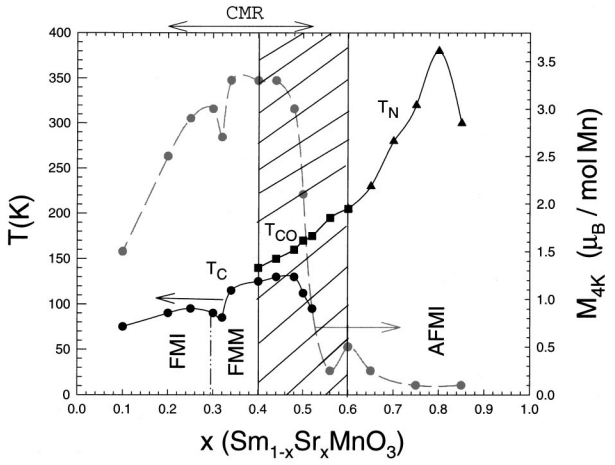

FIG. 4. Magnetic phase diagram of the $Sm_{1-x}Sr_xMnO_3$ line.

ionic size mismatch values. However the existence of CMR properties on the Mn^{3+} rich side for $L=$Pr and their absence for $L=$Sm emphasize the importance of $\langle r_A \rangle$ on the magnetoresistance.

C. $Sm_{1-x}Sr_xMnO_3$: Appearance of a FMM state in the hole doped region and CMR disappearance in the electron doped one

The study of the two above systems suggests strongly that $\langle r_A \rangle$ should be increased in order to increase W and thus to obtain a FMM state in the hole doped region. Such a condition can be fullfilled by replacing Ca^{2+} by Sr^{2+}. The perovskites $Sm_{1-x}Sr_xMnO_3$ correspond to larger $\langle r_A \rangle$ values, $\langle r_A \rangle$ increasing from 1.132 Å for $x=0$ to 1.31 Å for $x=1$. However, in this system the size mismatch is much larger than for both aforementioned systems, reaching a maximum value of 7.9×10^{-3} Å^2 at $x=0.5$.

The magnetic phase diagram of this series (Fig. 4) shows that the ferromagnetic domain has considerably grown, compared to SmCa and PrCa extending from $x=0.10$ to $x>0.5$. Moreover, metallicity has appeared for some x values, leading to two ferromagnetic domains, FMI with $0.10\leqslant x\leqslant 0.30$ and FMM with $0.30<x\leqslant 0.52$. This extension of the ferromagnetism and especially the appearance of the FMM state is explained by the increase of $\langle r_A \rangle$ and consequently of the Mn-O-Mn angle, i.e., of the band width W. Nevertheless the T_C values are not much larger than those obtained for the SmCa and PrCa systems, remaining smaller than 130 K, in agreement with the larger σ^2 values in the SmSr series.

For $x>0.6$, the SmSr manganites differ fundamentally from the SmCa and PrCa series, in particular the cluster glass behavior in the Mn^{4+} rich region is never observed. In this region T_N measured on the $M(T)$ curve is larger than the T_{CO} values observed for the SmCa and PrCa systems and increases dramatically with $\langle r_A \rangle$, culminating at about 380 K for $x=0.80$. It is not possible to date to discriminate the factors which govern T_N taken at the magnetization maximum.

For $0.4\leqslant x\leqslant 0.6$ at room temperature (RT), electron diffraction shows that two structural types coexist within every grain; both exhibit the same cell parameters ($a\sim c\sim a_p\sqrt{2}$ and $b\approx 2a_p$) but different Bravais lattices, mainly one is P type and the other is I type. The I/P ratio increases with x. At low temperature, 92 K, extra reflections are observed in incommensurate positions [Fig. 5(a)] in the P-type areas. The modulation vector is parallel to a^* with $q=0.35\,a^*$ for $x=0.5$. Note that the superstructure takes place along the two equivalent $[101]_P$ and $[10\bar{1}]_P$ directions of the perovskite subcell (see black triangles, the satellites being indexed using four indices $hklm$). The lattice image [Fig. 5(b)], which consists in a bidimensional system of fringes, clearly shows that the superstructure is not perfectly established throughout the whole matrix, but that modulated domains coexist with nonmodulated ones in the P-type areas. These ED patterns and lattice images evidence local cell distortions which are consistent with the local appearance of CO. By warming, the positions of the satellites vary and their intensity decreases, so that the positions of the satellites cannot be longer measured at $T>T_{CO}$. T_{CO} increases with x, from ~140 K for $x=0.4$ up to 205 K for $x=0.6$. This T_{CO} vs x dependence

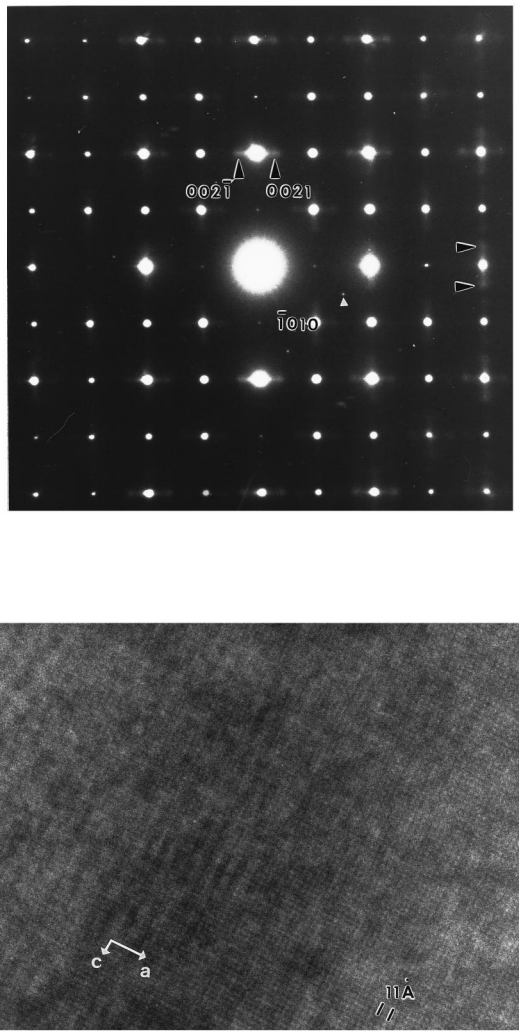

FIG. 5. [010] ED pattern (a) and corresponding lattice image (b) recorded at 92 K for $Sm_{0.5}Sr_{0.5}MnO_3$. The black arrows indicate the superstructure reflections (in incommensurate positions) probing the CO phenomenon. The small white triangle indicates a weak diffraction spot characteristic of the presence of a small [101] twinned domain.

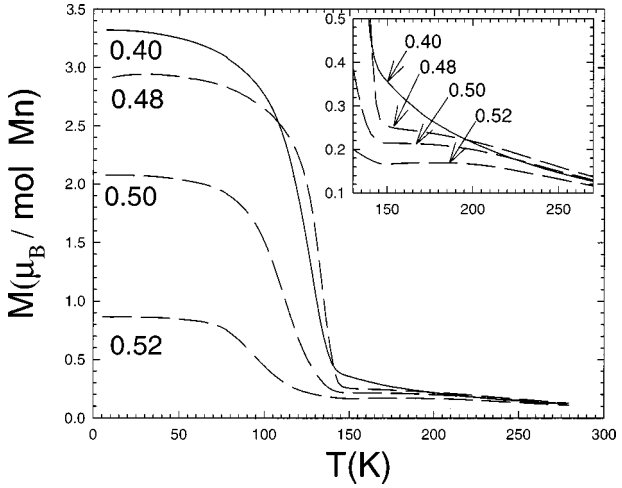

FIG. 6. $M(T)$ curves, in 1.45 T, for $Sm_{1-x}Sr_xMnO_3$ samples with $0.40 \leqslant x \leqslant 0.52$. Inset: enlargements above T_C showing the small bumps linked to weak AFM transitions.

shows that the modulated phase exists over a rather large x range. Structural and microstructural study of these compounds will be detailed elsewhere.

Consequently, the transition zone, sandwidched between the FMM and AFMI domains discussed above must be distinguished for $0.4 \leqslant x \leqslant 0.6$ (see hatched zone on Fig. 4). For this domain lying close to the half doped composition, the magnetization curves (Fig. 6) show the coexistence of two magnetic transitions as T decreases, PMI-AFMI and AMFI-FMM. Only a bump is observed on the $M(T)$ curves corresponding to the PM-AFM transition in agreement with the microscopy observations evidencing CO for only a part of the samples and a smooth transition from the CO to the disordered state. Note that these T_N values, though difficult to detect on these $M(T)$ curves, coincide rather well with the T_{CO} values detected from electron diffraction.

In contrast to the SmCa and PrCa systems, the SmSr manganites exhibit metal-insulator transition in the hole doped region. The low T_C values allow large resistivity values in the PMI state to be reached, just above T_C, so that large resistivity decreases by several orders of magnitude are obtained as the samples are cooled down below T_C in the FMM

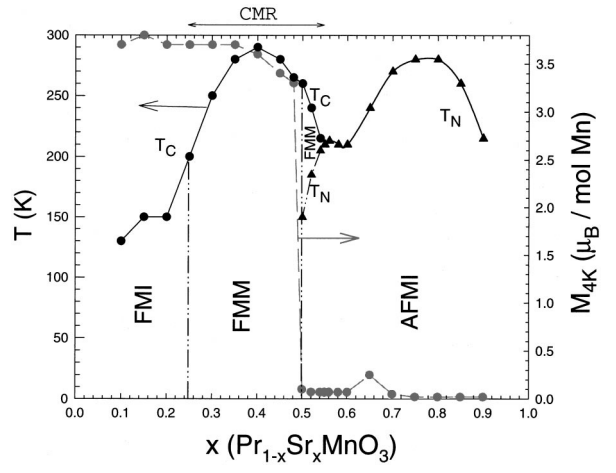

FIG. 7. Magnetic phase diagram of the $Pr_{1-x}Sr_xMnO_3$ series.

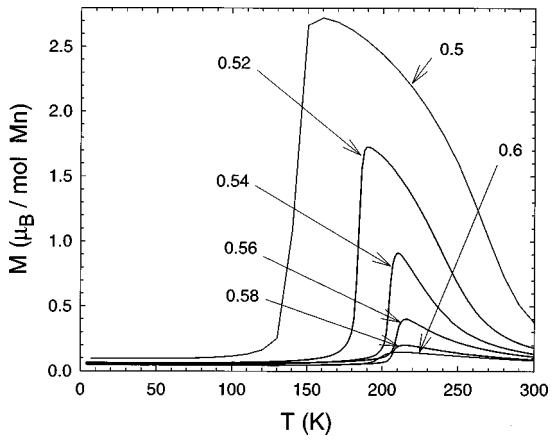

FIG. 8. $M(T)$ curves (recorded in 1.45 T) of selected compositions for the $Pr_{1-x}Sr_xMnO_3$ samples with $0.5 \leqslant x \leqslant 0.6$.

state. Consequently CMR properties are obtained for $0.30 \leqslant x \leqslant 0.52$, the highest resistance ratios being achieved for $x = 0.44$, as previously reported.[25]

D. $Pr_{1-x}Sr_xMnO_3$: Comparison with $La_{1-x}Ca_xMnO_3$

The magnetic phase diagram of this series $Pr_{1-x}Sr_xMnO_3$ (Fig. 7) is characterized, similar to that of $Sm_{1-x}Sr_xMnO_3$, by the existence of a large ferromagnetic domain extending from $x = 0.10$ to $x = 0.50$, in agreement with the large size of the A-site cations. As for SmSr we can distinguish two ferromagnetic domains, one FMI for $0.1 \leqslant x < 0.25$, and one FMM domain for $0.25 \leqslant x < 0.50$. The larger T_C values obtained for this system, compared to the SmSr manganites, originates from the larger $\langle r_A \rangle$ values which generate a larger W bandwidth and from the smaller mismatch σ^2.

For $0.50 \leqslant x \leqslant 0.55$ a narrow transition zone (Fig. 7) is obtained, which shows the coexistence of two magnetic transitions PMI-FMM and FMM-AFMI. However, no satellites are observed by ED between 92 K and RT, so that these samples cannot be considered as CO, the FMM-AFMI transition temperatures on the $M(T)$ curves are thus Néel temperatures. In this region, T_C decreases and T_N increases as x increases, so that the Mn^{3+}/Mn^{4+} mixed valency must be carefully controlled in order to go from the $M(T)$ curve of $Pr_{0.50}Sr_{0.50}MnO_3$ characterized by two magnetic transitions PMI-FMM-AFMI to the unique PMI-AFMI transition of $Pr_{0.4}Sr_{0.6}MnO_3$ (Fig. 8). For $x = 0.50$, the antiferromagnetic structure that appears in this region is of a different nature[26,27] from the one observed for the $L_{0.5}Ca_{0.5}MnO_3$ compounds with L = La,Pr.[22,28,29] $Pr_{0.5}Sr_{0.5}MnO_3$ exhibits an A-type structure with a $d_{x^2-y^2}$ orbital ordering, instead of CE type and d_{z^2} orbital ordering for $Pr_{0.5}Ca_{0.5}MnO_3$.

For $0.55 < x \leqslant 0.90$, a large AFMI domain is obtained, similarly to the SmSr manganites. Nevertheless, the evolution of T_N vs x is different. It keeps a rather constant value for $0.55 \leqslant x \leqslant 0.60$ and then strongly increases reaching a maximum value of 285 K at $x = 0.75$ (Fig. 7), i.e., significantly smaller than the maximum T_N value (380 K) obtained for the SmSr manganites (Fig. 4). For these compositions, a clear increase of the resistivity is observed at T_N [as exemplified Fig. 9(a) for $x = 0.8$] showing the localizing character of the PMI-AFMI transition which may be attributed to the

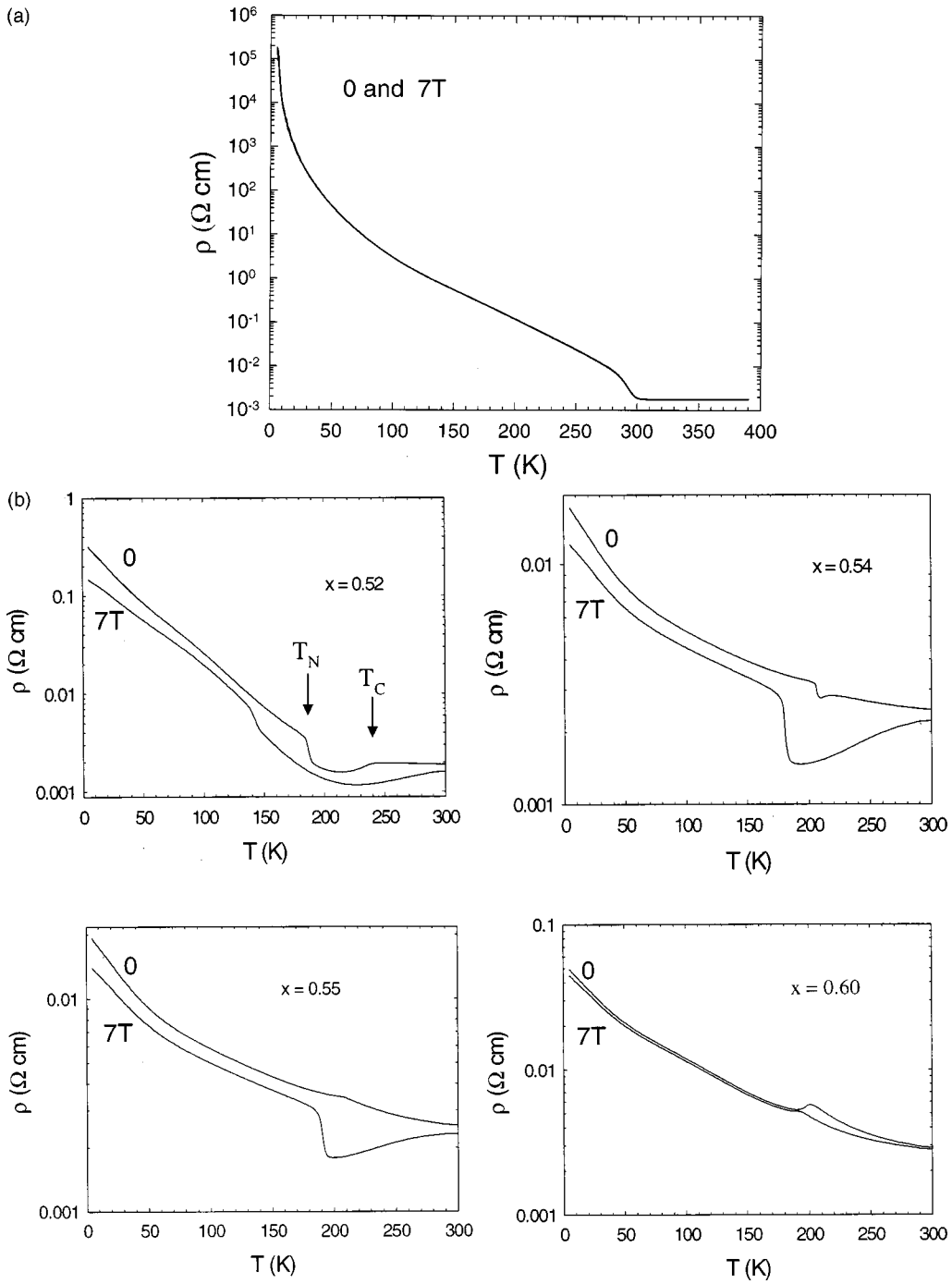

FIG. 9. (a) $\rho(T)$ curves ($H=0$ and 7 T) for $Pr_{0.2}Sr_{0.8}MnO_3$. (b) $\rho(T)$ registered in magnetic fields of 0 and 7 T (field cooling) for $Pr_{1-x}Sr_xMnO_3$ compositions with $0.5 \leqslant x \leqslant 0.6$.

d_{z^2} orbital ordering into chains of the *C*-type AFM structure. It has indeed been shown for $x=0.50$ (Refs. 26 and 27) and $x=0.60$ (Ref. 30) that the same *A*-type AFM structure is obtained in contrast to $Nd_{1-x}Sr_xMnO_3$ which can exhibit an *A* or CE-type AFM structure in the same composition range ($x=0.50$ and 0.6).[31] In the region $0.60<x<0.90$, T_N goes through a maximum, $T_N=285$ K for $x\sim0.75$. The different x dependence of T_N between $0.55 \leqslant x \leqslant 0.6$ and $0.6<x<0.9$ may be related to a change of AFM structure, a *C*-type AFM structure is reported, for instance, for $Pr_{0.15}Sr_{0.85}MnO_3$.[20]

In this system, CMR properties are observed for all the FMM domain, i.e., for $0.25<x<0.50$. However, for the $0.50 \leqslant x \leqslant 0.55$ compositions, characterized by two magnetic transitions at T_C and T_N, there exist two kinds of magnetoresistance. Near T_C, the resistivity is decreased by the magnetic field application leading to the same magnetoresistance effect as for $0.25<x<0.50$. The second kind of MR occurs in the T_N vicinity, the AFMI state can be molten into a FMM one by magnetic field application as shown for $x=0.52$ in Fig. 9(b). Nevertheless, for $x>0.55$, the AFMI

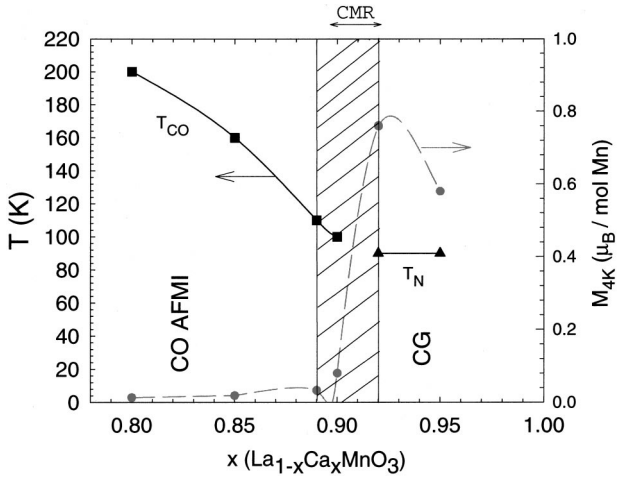

FIG. 10. Magnetic phase diagram of $La_{1-x}Ca_xMnO_3$ samples with x values limited to the electron doped region where CMR properties are shown.

cannot be easily collapsed due to the lack of DE ferromagnetic interactions, decreasing thus the MR effect as shown for $Pr_{0.4}Sr_{0.6}MnO_3$ [Fig. 9(b)].

The phase diagram of $Pr_{1-x}Sr_xMnO_3$ exhibits great similarities with that of $La_{1-x}Ca_xMnO_3$ previously established by Schiffer *et al.*,[10,11] and that we have completed on the Mn^{4+}-rich side (Fig. 10). The FM area in the LaCa system, subdivided into two FMI and FMM regions, extends similarly over a wide range of compositions up to $x=0.49$, and the FMM region is also large ($0.17 \leqslant x \leqslant 0.49$).[10,11] In the FMM region of both series, PrSr and LaCa manganites, T_C increases first and goes through a maximum value around a same hole concentration $x=0.35-0.40$. It must be stressed that the $T_C=260$ K maximum value for LaCa is higher than that of SmSr, $T_C=130$ K, though the $\langle r_A \rangle$ values of the latter are larger. This is easily explained by considering the *A*-site cationic size mismatch which is much smaller for LaCa, 3.2×10^{-4} Å^2, against 7.9×10^{-3} Å^2 for SmSr, and thus favors the ferromagnetic state. By going from SmSr to PrSr, $\langle r_A \rangle$ increases whereas σ^2 decreases so that T_C of the latter is shifted up, reaching thus values close to the LaCa ones, though the $\langle r_A \rangle$ of the latter are smaller.

The similarity of the FM regions for the LaCa and PrSr series explains why the LaCa manganites exhibit CMR properties, in the FMM regions, i.e., for $0.17 \leqslant x \leqslant 0.50$, as the PrSr manganites ($0.25 \leqslant x \leqslant 0.55$). In contrast to the PrSr oxides, the LaCa manganites exhibit a CO-AFMI region below T_{CO}. The $T_{CO}(x)$ of LaCa and $T_N(x)$ of PrSr curves are characterized by a similar shape (compare Fig. 7 with the diagrams of Refs. 10 and 11) with a maximum of T_{CO} (260 K) around $x=0.65$ for LaCa (against $T_N=285$ K for $x=0.75$ for PrSr). This difference, CO or not, is due to the fact that $\langle r_A \rangle$ decreases as x increases for LaCa, contrary to PrSr. Large *A*-site cations 1.18 to 1.31 Å are obtained for PrSr whereas the smaller *A*-site cations (1.216 to 1.18 Å) in LaCa favor the CO structure. The LaCa system differs from the PrSr phase by the existence of a cluster glass domain on the Mn^{4+} rich side for $x \geqslant 0.9$ (Fig. 10). The latter is similar to that observed for other $L_{1-x}Ca_xMnO_3$ electron doped manganites (Figs. 1 and 3), requiring a small size of the *A*-site cation. Thus, at the borderline of this cluster glass

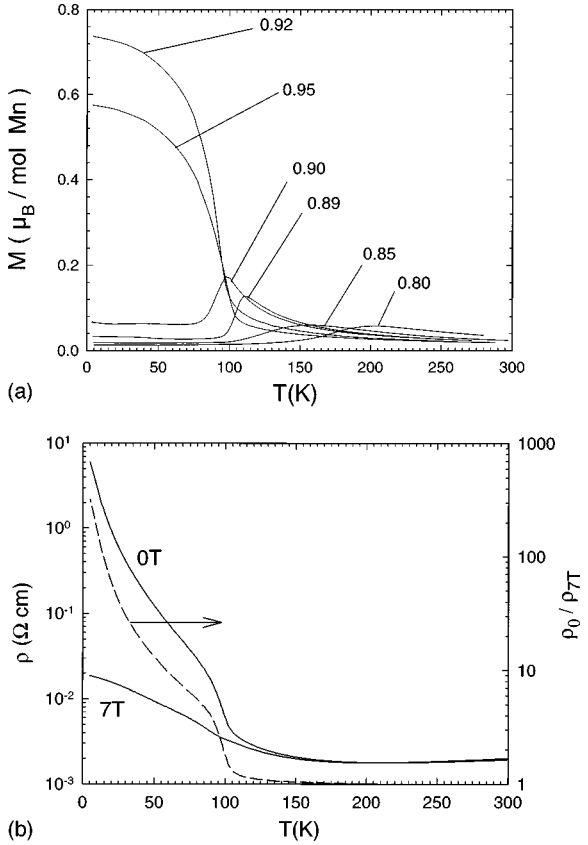

FIG. 11. (a) $M(T)$ curves (in 1.45 T) of $La_{1-x}Ca_xMnO_3$ compositions with $0.80 \leqslant x \leqslant 0.95$. (b) $\rho(T)$ curves ($H=0$ and $H=7$ T) for $La_{0.10}Ca_{0.90}MnO_3$.

domain, i.e., for $x \cong 0.90$, a competition between FM and AFM is observed on the $M(T)$ curve [Fig. 11(a)] and consequently the CMR effect is obtained as shown from the $\rho(T)$ curves under 0 and 7 T [Fig. 11(b)].

IV. DISCUSSION AND CONCLUDING REMARKS

From the comparison of these magnetic phase diagrams of $L_{1-x}A_xMnO_3$ manganites, it appears clearly that there is no symmetry between the hole doped and electron doped regions, concerning the magnetic and transport properties.

The first important feature deals with the fact that ferromagnetism appears systematically for low hole concentrations, i.e., for x close to 0.1 whatever L and whatever A, calcium or strontium. At this hole concentration, the manganite is insulating. For $A=$Ca, the FMI state extends over a rather wide hole concentration range ($\sim$0.10–0.35) and is followed by the CO-AFMI region ($0.35 \geqslant x > 0.80$), whereas for $A=$Sr the FMI-FMM transition is observed.

The second remarkable point concerns then the appearance of the ferromagnetic metallic state. The FMM state appears only for a sufficiently large size of the *A* site cation, allowing a large band (W) to be generated and beyond a certain value of the hole concentration. For this reason, the SmCa and PrCa manganites which contain too small *A*-site cations have a too narrow band and do not form FMM domains, in contrast to LaCa, SmSr, and PrSr manganites. The T_C of these FMM manganites is always larger than that of

the FMI phases. For these FMM phases a bell shaped curve $T_C(x)$ is systematically observed whatever the *A*-site cations with a maximum at $x=0.35-0.40$, showing that the hole concentration plays a dominant role upon T_C. This was first shown by Jonker *et al.* who found that for $x\sim0.33$ the Mn^{3+}-O-Mn^{4+} double exchange is the most efficient.[32] For this critical *x* value, $(T_C)_{max}$ will be the higher for large $\langle r_A\rangle$ and smaller σ^2 values as previously shown. [13–16] The homogeneity range of the FMM state is systematically limited for the superior limit around $x\sim0.50$, whereas, in contrast, the inferior limit varies significantly with the nature of the *A*-site cations from $x=0.17$ for LaCa (Ref. 10) to $x=0.30$ for SmSr.

The nature of the low-temperature phase, that appears for higher *x* values ($x>0.50$) is also an important topic. Two kinds of behaviors must be distinguished, depending on the size of the *A*-site cations. For small *A*-site cations, i.e., $L_{1-x}Ca_xMnO_3$, charge ordering phenomena appear, in the form of Mn^{3+} and Mn^{4+} stripes,[5,24,33] and the CO region coincides with the CE or *C*-type AFMI domain with $T_{CO}>T_N$.[22] The CO-AFMI state can start to develop in the hole doped region competing with the expansion of the FMM state, and extends in the electron doped region over a broad composition range, as shown for instance in the SmCa series for which the CO-AFMI state extends from $x\approx0.4$ to $x\approx0.80$. The second kind of behavior, which is observed for the series of larger cations $L_{1-x}Sr_xMnO_3$ corresponds to the disappearance of the CO state on a broad range of composition in the electron doped region. For the larger *A*-site cations, there exists a particular zone in the phase diagram around the half doped composition ($x\sim0.5$) where two magnetic transitions coexist. This is the case of SmSr and PrSr systems, which show an opposite behavior with $T_N\geqslant T_C$ and $T_N\leqslant T_C$, respectively. As a result, $Sm_{0.5}Sr_{0.5}MnO_3$ is a ferromagnetic metal below $T_C=100$ K, whereas $Pr_{0.5}Sr_{0.5}MnO_3$ is a ferromagnetic metal only between T_C (260 K) and T_N (150 K). These results show clearly that in this region, the magnetotransport properties can be drastically changed only by replacing praseodymium by samarium or vice versa. This viewpoint is confirmed by the study of the solid solution $Sm_{0.5-x'}Pr_{x'}Sr_{0.5}MnO_3$. Starting from $x'=0$, a clear increase of T_C has indeed been observed as x' increases. This is illustrated by the $M(T)$ and $\rho(T)$ curves (in 0.01 T) of some samples (Fig. 12), T_C becoming larger than T_N for $x'=0.15$, so that a CO-AFMI state is induced at low temperature for these composition as shown from magnetic and ED studies, in contrast with the *A*-type AFM of $Pr_{0.5}Sr_{0.5}MnO_3$ ($x'=0.5$). This great influence of $\langle r_A\rangle$ upon the appearance or disappearance of FMM and AFMI state in this region is at the origin of the existence of CMR effects, the CO-AFMI state being easily collapsed into the FMM state under a magnetic field as shown from the $\rho(T)$ curves under 0 and 7 T for $x'=0.18$ [Fig. 12(b)].

The appearance of ferromagnetism concomitantly with metallicity in the electron doped region ($x>0.85$ for SmCa, $x>0.9$ for LaCa) is also a remarkable result, showing that such a phenomenon can only appear for small *A*-site cations (in the LnCa series). In this composition range, the compounds exhibit a cluster glass behavior and the NPD study has evidenced a ferromagnetic component in a *G*-type AFM

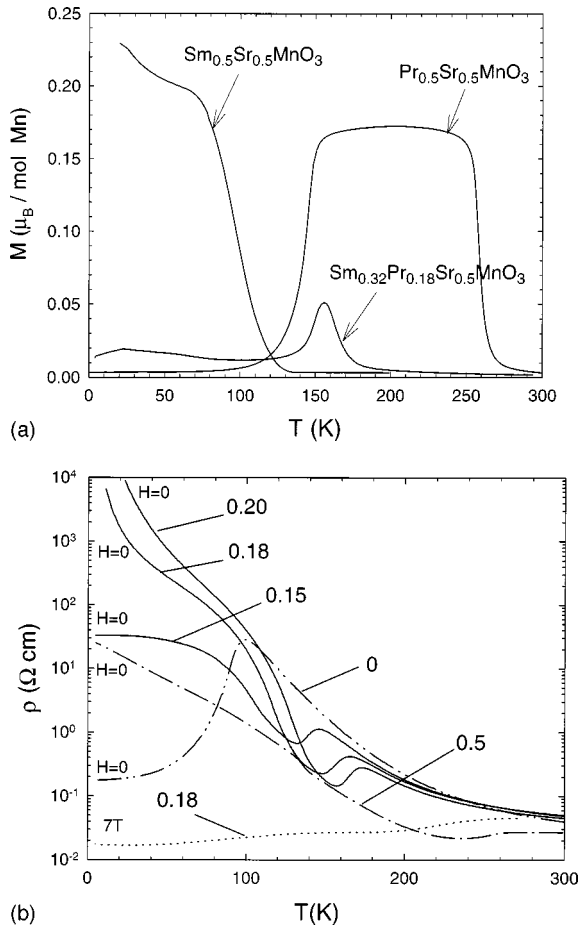

FIG. 12. (a) $M(T)$ curves, registered in 0.01 T, for $Sm_{0.5-x'}Pr_{x'}Sr_{0.5}MnO_3$ samples ($x'=0$, 0.18, and 0.5). (b) $\rho(T)$ curves ($H=0$) for the $Sm_{0.5-x'}Pr_{x'}Sr_{0.5}MnO_3$ series and the $\rho(T)$ curve with $H=7$ T for $x'=0.18$.

matrix which may indicate a phase segregation. Such an observation may be of great importance to support the phase segregation scenario predicted by Moreo *et al.*[34] for the Mn^{4+} rich compositions in the LaCa system on the basis of theoretical calculations.

These phase diagrams allow the compositions for which CMR effect will appear to be predicted. The coexistence of ferromagnetism and metallicity is a very important factor for the appearance of MR. Thus, in hole doped regions, CMR effects will be obtained in the whole FMM domains corresponding to large $\langle r_A\rangle$ values as shown for SmSr, PrSr, NdSr, and LaCa manganites. For each series, the best effect is obtained for a composition range which is $\langle r_A\rangle$ dependent. In the same way, CMR will be obtained for small $\langle r_A\rangle$ values, in the electron doped region close to the cluster glass region, $x\sim0.82-0.90$, where FM and AFM are competing, i.e., for SmCa, PrCa, and LaCa manganites. Finally, the CMR effect can also appear at the boundary of the FM state, in the hole doped charge ordered state, provided that the latter is metastable due to the small size of the interpolated of the *A*-site cation (close to 1.18 Å), as shown for PrCa manganites ($0.30\leqslant x\leqslant0.45$).

[1] C. Zener, Phys. Rev. **82**, 403 (1951).
[2] P. G. de Gennes, Phys. Rev. **118**, 141 (1960).
[3] J. B. Goodenough, Prog. Solid State Chem. **5**, 149 (1971).
[4] R. M. Kusters, J. Singleton, D. A. Keen, R. Mc Greevy, and W. Heyes, Physica B **155**, 362 (1989).
[5] See *Colossal Magnetoresistance, Charge Ordering and Related Properties of Manganese Oxides*, edited by B. Raveau and C. N. R. Rao (World Scientific, Singapore, 1998).
[6] H. Chiba, M. Kikuchi, K. Kusaba, Y. Muraoka, and Y. Syono, Solid State Commun. **99**, 499 (1996).
[7] I. O. Troyanchuk, N. V. Samsonenko, H. Szymczak, and A. Nabialek, J. Solid State Chem. **131**, 144 (1997).
[8] C. Martin, A. Maignan, F. Damay, M. Hervieu, and B. Raveau, J. Solid State Chem. **134**, 198 (1997).
[9] A. Maignan, C. Martin, F. Damay, and B. Raveau, Chem. Mater. **10**, 950 (1998).
[10] P. Schiffer, A. P. Ramirez, W. Bao, and S. W. Cheong, Phys. Rev. Lett. **75**, 3336 (1995).
[11] A. P. Ramirez, S. W. Cheong, and P. Schiffer, J. Appl. Phys. **81**, 5337 (1997).
[12] R. Mahesh, R. Mahendiran, A. K. Raychaudhuri, and C. N. R. Rao, J. Solid State Chem. **114**, 297 (1995); **120**, 204 (1995).
[13] H. Y. Hwang, S. W. Cheong, P. G. Radaelli, M. Marezio, and B. Batlogg, Phys. Rev. Lett. **75**, 914 (1995).
[14] A. Maignan, Ch. Simon, V. Caignaert, and B. Raveau, Solid State Commun. **96**, 623 (1995).
[15] L. M. Rodriguez-Martinez and J. P. Attfield, Phys. Rev. B **54**, 15 622 (1996).
[16] F. Damay, C. Martin, A. Maignan, and B. Raveau, J. Appl. Phys. **82**, 6181 (1997).
[17] A. Sundaresan, A. Maignan, and B. Raveau, Phys. Rev. B **56**, 5092 (1997).
[18] M. Hervieu, A. Barnabé, C. Martin, A. Maignan, F. Damay, and B. Raveau, Eur. Phys. J.: Appl. Phys. **138**, 31 (1999).
[19] A. Maignan, C. Martin, F. Damay, B. Raveau, and J. Hejtmanek, Phys. Rev. B **58**, 2758 (1998).
[20] C. Martin, A. Maignan, M. Hervieu, B. Raveau, Z. Jirak, A. Kurbakov, V. Trounov, G. André, and F. Bourée, J. Magn. Magn. Mater. (to be published).
[21] C. Martin, A. Maignan, M. Hervieu, B. Raveau, Z. Jirak, G. André, and F. Bourée (unpublished).
[22] Z. Jirak, S. Krupicka, Z. Simsa, M. Dlouha, and S. Vratislav, J. Magn. Magn. Mater. **53**, 153 (1985).
[23] Y. Tomioka, A. Asamitsu, H. Kuwahara, Y. Moritomo, and Y. Tokura, Phys. Rev. B **53**, 1689 (1996).
[24] M. Hervieu, A. Barnabé, C. Martin, A. Maignan, and B. Raveau, Phys. Rev. B **60**, R726 (1999).
[25] F. Damay, N. Nguyen, A. Maignan, M. Hervieu, and B. Raveau, Solid State Commun. **98**, 997 (1996).
[26] H. Kawano, R. Kajimoto, H. Yoshizawa, Y. Tomioka, H. Kuwahara, and Y. Tokura, Phys. Rev. Lett. **78**, 4253 (1997).
[27] F. Damay, C. Martin, M. Hervieu, A. Maignan, and B. Raveau, J. Magn. Magn. Mater. **184**, 71 (1998).
[28] E. O. Wollan and W. C. Koehler, Phys. Rev. **100**, 545 (1955).
[29] J. B. Goodenough, Phys. Rev. **100**, 564 (1955).
[30] C. Martin, M. Hervieu, A. Maignan, and B. Raveau (unpublished).
[31] H. Kuwahara, T. Okuda, Y. Tomioka, T. Kimura, A. Asamitsu, and Y. Tokura, in *Science and Technology of Magnetic Oxides*, edited by M. Hundley *et al.*, MRS Symposia Proceedings No. 494 (Materials Research Society, Pittsburgh, 1998), p. 83.
[32] G. H. Jonker and J. H. Van Santen, Physica (Amsterdam) **16**, 337 (1950).
[33] C. H. Chen and S. W. Cheong, Phys. Rev. Lett. **76**, 4042 (1996).
[34] A. Moreo, S. Yunoki, and E. Dagotto, Science **283**, 2034 (1999).